Analytica Chimica Acta 1267 (2023) 341226

Contents lists available at ScienceDirect

Analytica Chimica Acta

journal homepage: www.elsevier.com/locate/aca

An impedance based microfluidic sensor for evaluation of individual red blood cell solute permeability

Lining Huang [a], Ibrahim Jasim [a], Omar Alkorjia [a], Cansu Agca [b], Anna Oksman [c], Yuksel Agca [b], Daniel E. Goldberg [c], James D. Benson [d,**,1], Mahmoud Almasri [a,*,1]

[a] Department of Electrical Engineering and Computer Science, University of Missouri-Columbia, MO, USA
[b] Department of Veterinary Pathology, University of Missouri-Columbia, MO, USA
[c] Department of Medicine, Division of Infectious Diseases, and Department of Molecular Microbiology, Washington University School of Medicine, Saint Louis, MO, 63130, USA
[d] Department of Biology, University of Saskatchewan, Saskatoon, SK, Canada

HIGHLIGHTS

- Rapid identification of individual red blood cells infected with P. falciparum malaria parasites.
- RBC membrane permeability was measured in individual cells.
- The microfluidic sensor was calibrated and validated for sizing cells and beads.
- RBCs were measured in 0.19 s after mixing with anisosmotic media from separate inlets at 5 electrodes over 1.3 s.
- The focusing electrode pair lined up the RBCs in the centerline of the channel using p-Dep forces.

GRAPHICAL ABSTRACT

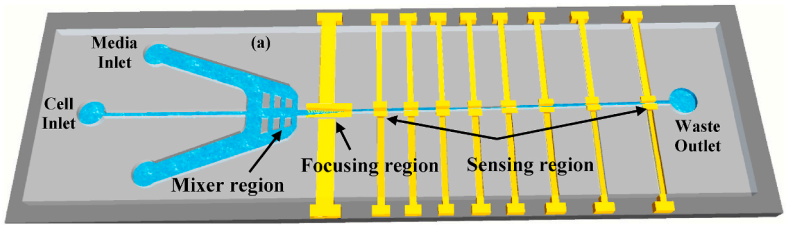

ARTICLE INFO

Handling Editor: Dr. J.P. Landers

Keywords:
Sensors
Malaria detection
Microfluidic
Red blood cell
Permeability
Boyle Van't Hoff
Impedance

ABSTRACT

—In this paper, we investigate a microfluidic based sensing device for cell membrane permeability measurements in real time with applications in rapid assessment of red blood cell (RBC) quality at the individual cell level. The microfluidic chip was designed with unique abilities to line up the RBCs in the centerline of the microchannel using positive dielectrophoresis (p-DEP) forces, rapid mixing of RBCs with various media (e.g. containing permeating or nonpermeating solutes) injected from different inlets to achieve high mixing efficiency. The chip detects the impedance values of the RBCs within 0.19 s from the start of mixing with other media, at ten electrodes along the length of the channel and enables time series measurements of volume change of individual cell caused by cell osmosis in anisosmotic fluids over a 0.8 s postmixing timespan. This technique enables estimating water permeability of individual cell accurately. Here we first present confirmation of a linear voltage-diameter relationship in polystyrene bead standards. Next, we show that under equilibrium conditions, the voltage-volume relationship in rat red blood cells (RBCs) is linear, corresponding to previously published Boyle van 't Hoff plots. Using rat cells as a model for human, we present the first measurement of water permeability in individual red blood cells and confirm that these data align with previously published population level values for human RBC. Finally, we present preliminary evidence for possible application of our device to

* Corresponding author.
** Corresponding author.
E-mail addresses: james.benson@usask.ca (J.D. Benson), almasrim@missouri.edu (M. Almasri).
[1] corresponding authors contributed equally.

https://doi.org/10.1016/j.aca.2023.341226
Received 3 December 2022; Received in revised form 10 April 2023; Accepted 17 April 2023
Available online 11 May 2023

identify individual RBCs infected with Plasmodium falciparum malaria parasites. Future developments using this device will address the use of whole blood with non-homogenous cell populations, a task currently performed by clinical Coulter counters.

1. Introduction

Transfusions of whole blood or individual components which include red blood cells (RBCs), platelets, and plasma are needed to restore blood volume to adequate levels after a loss of blood due to trauma or illness. About 118.54 million blood units are collected globally every year [1], including 13.6 million units of blood are administered in the U.S. The Food and Drug Administration (FDA) allows packed RBCs to be refrigerated for up to 42 days to allow blood centers the flexibility to manage the blood supply [2]. However, refrigerated storage duration of transfused blood is associated with multiple organ failure after injury [3].

During conventional refrigerated blood bank storage, alterations to blood components accumulate, and are known as 'Storage lesion'. This storage lesion increases RBC adhesion to endothelial cells and hemolysis and includes (1) metabolic and (2) shape changes [4]; (3) oxidative damage and membrane loss that leads to rheological changes (stiffer cells) and as well as alteration of lipids and proteins; (4) changes in the delivery and affinity of oxygen; and (5) shedding of active proteins and lipids (the formation of microvesicles). Stored RBCs undergo progressive morphological changes from the native deformable biconcave disk form to spherocytes with protrusions and finally to echinocytes. Together, these changes affect the stored RBCs in terms of deformability and results in negatively the premature removal of the RBCs from circulation [5–8]. Somewhat similarly, malaria is a parasitic infection of RBC marked by a significant change in the ability for the RBCs to deform when subjected to shear stress [9,10]. For example, the *Plasmodium falciparum* parasite, the most deadly human malaria parasite, transform through morphologically distinct stages within the RBCs, becoming progressively less deformable (stiffer) at each stage [11].

Deformability is manifested in key biophysical quantities including volume, sphericity, the surface area to volume ratio (SA:V), membrane lipid makeup, and osmotic fragility [12], and these characteristics are associated with RBC storage lesion. In particular, all of these RBC storage lesion phenomena will be manifested in two factors: (1) SA:V ratio [12]; (2) membrane lipid composition changes [13,14]. Moreover, after infection with the malaria parasite, RBCs progress through several distinct stages associated with similar and dramatic changes to RBC morphology affecting SA:V and lipid content [11]. In fact, we have previously shown theoretically that surface area to volume ratio linearly affects the time course of the process when exposing RBCs to anisosmotic permeating solutes, and the effective membrane permeability parameters only alter maximal and minimal volume points [15]. So, measuring RBC volumetric responses to anisosmotic media will, through biophysical analysis, indirectly inform assessment of membrane lipid and protein configuration and RBC sphericity–two critical components of cell quality. Both can be monitored and measured using our microfluidic device by exposing RBCs to anisosmotic media.

Current methods for quantifying RBC responses to anisosmotic solutions operate at the population-level. One method is using a benchtop particle counter, such as a Coulter counter. In this method, cells are mixed rapidly with a medium of different osmolality and their resulting volume changes are monitored [16]. These volume changes, however, are single measurements of many individual cells at single time points, and the time series is constructed by measuring many cells at many time points. This has the benefit of showing the mean population response, but obfuscates subpopulation responses, and is subject to the differences among mean and median responses that could help identify pathological responses. An additional challenge for benchtop coulter counters is that there is a near-second-long injection artifact that precludes accurate measurement in the critical time that RBC respond to aniosmotic medium. The second method uses a stopped flow apparatus [17], where RBC suspensions are rapidly mixed in a chamber and either the volume-dependent side scatter is tracked [18], or more recently the concentration dependent autofluorescence of hemoglobin is monitored [19]. These are indirect measures of volume of the whole population as a function of time that rely on the linearity of the fluorescence vs volume relationship, and as such are unable to quantify individual cell permeabilities.

Malaria is a devastating disease that afflicts hundreds of millions and kills an estimated six hundred thousand each year, mostly children in Sub-Saharan Africa, and Southeast Asia [20,21]. According to the WHO 3.4 billion people globally were estimated to remain at risk of malaria infection [22]. The deadliest species, *P. falciparum*, produces disease that can progress rapidly from symptoms to death. Rapid and accurate diagnosis is essential for the elimination of the disease. Medical care resources are limited in most endemic areas and diagnosis depends on time-consuming/insensitive microscopy or on rapid diagnostic tests (RDTs) [23]. The most sensitive of these RDTs detect the presence of a malaria parasite protein, histidine-rich protein II (HRPII), in the blood. These tests are inexpensive and take only a few minutes to make an accurate diagnosis. More than 200 million RDTs are employed each year. Unfortunately, the utility of these diagnostics is threatened by the appearance of HRP-negative parasites in patients. These gene deletion parasites grow normally, have normal fitness, have become prevalent in parts of South America [24,25], and can now be found in Africa [26]. Case reports of deletion strains in Asia have started to appear [27,28]. Modeling studies have suggested that use of RDTs has actually selected for the spread of HRP-deletion parasites, due to undertreatment and delays in treatment leading to increased transmission [28]. This situation has become a threat to malaria control efforts. There is a desperate need for new diagnostic modalities that are rapid, simple, and cheap. Current RDTs detect parasites at levels ranging from 1 to 100 parasites per μl [29]. Microscopy techniques require considerable training, management, equipment for light microscopy, and are associated with high false-negative rates. However, these techniques are able to detect HRP negative parasite infections. Microscopy is less sensitive, with detectable parasitemia levels ranging from 5 to 500 parasites per μl, a number that depends on the time the microscopist takes to inspect high magnification fields–a trained microscopist can review approximately 40 slides per workday [30] The long term goal of our current work is to provide a rapid and inexpensive initial screen for HRP positive or negative infections that requires little to no training and little to no equipment with comparable detection rates as microscopy. This will require a throughput of $\sim 10^4$ cells per test, though, similar to microscopy, additional time with our device will yield additional sensitivity.

In previous work, we developed and tested a preliminary design of a single-cell electronic particle counter device. This prototype device was the first to identify the permeability of common baker's yeast (*Saccharomyces cerevisiae*) individual cells without the use of microscopy or fluorescence and demonstrated the accuracy of the volume-voltage response in this microfluidic system. However, there were several design aspects needing significant improvements before use in RBCs. In particular, the time and efficiency of mixing the cells with anisosmotic medium is critical to identify permeability of rapidly responding cell types such as RBCs [31]. Therefore, to meet the potential need of more precise measurements of individual RBC quality, and also the possibility of microscopy and reagent free assessment of malaria in RBCs, the goal of this manuscript is to significantly redesign the MEMS single-cell particle sizer and validate and test using microbeads and RBCs. Therefore, this project presents the design, simulation, fabrication and

characterization of a proof-of-concept fluidic and impedance sensor/lab on a chip for measurements of real time cell membrane permeability at the single cell level. Once this device is validated, efforts to translate this technology into a form factor that could potentially function as a facile clinical tool can be undertaken: our goal is to allow for the use of minimally processed whole blood products in a self-contained or even hand-held clinical analysis tool.

2. Design and modeling

For our proof-of-concept, we made design considerations for application in isolated RBCs. To wit, the impedance based microfluidic sensor was designed, modeled, and simulated to monitor the volume changes of single RBCs versus time after mixing suspended RBCs with a different medium within 0.19 s from the start of mixing. The sensor was also used for the cell counting and volume sorting features. A 3-dimensional (3D) drawing of the biosensor is shown in Fig. 1. The sensor consists of three novel regions, which includes a passive microfluidic mixer region to mix the RBCs with extracellular media, a focusing region to line up the RBCs in the centerline of the microchannel, and a sensing region to measure the impedance change (volume change) versus time. The structural design of the microfluidic mixer region ensures excellent mixing efficiency, and the new focusing region design lines up the RBCs in the centerline of the microchannel and ensuring repeatable concentration vs time in the microchannel to eliminate the possibility of clogging the sensing region immediate extracellular surrounding for each cell. Moreover, the sensing region's geometry was redesigned to accommodate the study of RBCs.

As shown in Fig. 1, the sample is introduced into the sensor sample inlet, located in the center microchannel, while the reactant medium, e.g., different concentrations of phosphate buffer saline (PBS) or the permeating solute dimethyl sulfoxide (DMSO), was introduced into the sensor from the outer two inlets converging to form a wide (150 μm) T-shaped microchannel with the center cell suspension channel (50 μm), and three narrower multi-vertical microchannels (width 30 μm) that feed directly to the straight channel (length 400 μm, width 100 μm), forming the passive mixer region (Fig. 1). The RBCs and reactant medium mixture continued to flow toward the focusing microchannel, made of a vertical sidewalls and thin Au fingers that were designed with a 45° tilting angle. The focusing region was used to align the RBCs in the center of the microfluidic channel, and which will continue to move toward the sensing region that has a width three times narrower than that of the ending of focusing channel. The fluid will exit from the sample waste outlet. To investigate an individual RBC's changing volume versus time after exposure to extracellular media, we have patterned 10 electrodes in the sensing region microchannel, where each vertical electrode measures and record the impedance of RBC (thus, indirectly, volume) at the time it passed through. The electrodes were distributed along the detection channel such that more frequent measurements were taken at the initial portion of the channel, where most of volume change of the cell happens [19].

2.1. Microfluidic mixing region modeling

We have selected a passive mixer design that induces an efficient mixing of the RBCs in PBS with different extracellular media, e.g., PBS at various concentrations, with a short mixing time. The mixer consists of cell suspension flow channel (width 50 μm), two microchannels (width 150 μm), i.e., 3x larger and forming a T-shaped structure for loading extracellular media, three narrower multi-vertical channels (each with a width of 30 μm). These microchannels feed directly to the straight microchannel with 400 μm width and 100 μm length, forming the passive mixer region. The extracellular channel was designed to intersect with the cell flow channel in the normal direction to increase the interface between the RBCs and the extracellular media. In comparison with a serpentine microchannel mixer, this design has resulted in a higher mixing efficiency while decreasing the mixing time to achieve higher system sensitivity. Although the serpentine shaped microchannel

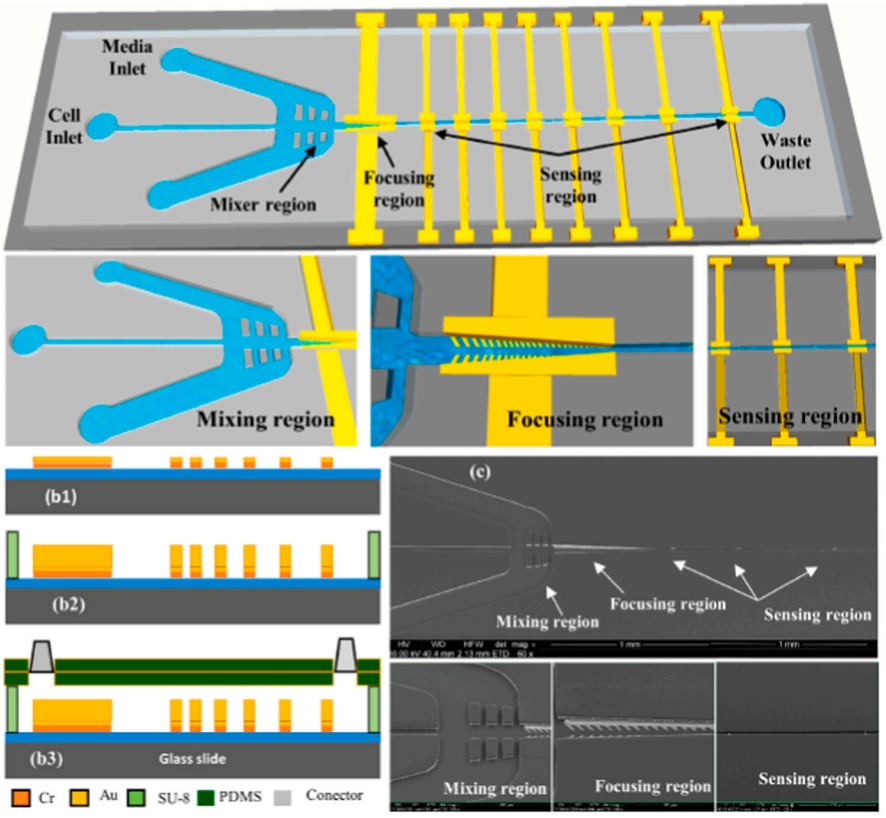

Fig. 1. (a) 3-dimensional schematics showing the microfluidic based impedance sensor for sensing and monitoring the volume change of individual RBCs, and a magnified view of the three regions. The microfluidic microchannel (Color in blue) consists of three regions; microfluidic mixing, cell focusing, and cell sensing regions. In addition, the device was designed with three inlets; one is used for introducing RBCs located in the center channel, and two extracellular media inlets located on the outer two channels, and one waste outlet. (b) Schematics of the processing steps used for fabricating the microfluidic sensing chip. (c) SEM micrographs of sensing device along with magnified views of the three regions. (For interpretation of the references to color in this figure legend, the reader is referred to the Web version of this article.)

can achieve a 100% mixing efficiency, it increases the microchannel length and thus increased the mixing time much more than the present implementation, an important consideration because the volume of RBCs starts to change as soon as it begins mixing with anisosmotic medium. Therefore, the serpentine microchannel, that was used in our previous generation sensors, was eliminated, and instead added six pillars which occupies shorter microchannel length. The use of six pillars has increased the mixing interface area and introduced some additional chaotic advection achieving better mixing efficiency while reducing the microchannel length resulting in a shorter mixing time. The contribution of the six pillars is minimum in comparison with the 150 μm microchannel, but still it improved the mixing efficiency by an additional 2.45%.

The microfluidic mixer region was modeled and simulated under a steady-state condition using COMSOL finite element tool (COMSOL Multiphysics). The concentrations of the center inlet (blue in color) and two outer inlets (red in color) were selected to be 0 mol/m^3 and 50 mol/m^3, respectively. We have also selected an incompressible and laminar fluid flow with non-slip boundary conditions. The mixing efficiency and mixing time were simulated versus flow rate using COMSOL. Fig. 2(a) shows the mixing of two dyes, mixing efficiency and mixing time. To determine the mixing time, the fluid velocity was simulated at each flow rate across the device length, e.g., the fluid velocity in the straight part of the microchannel was increased from 3 mm/s to 8 mm/s, with an average speed of 5.5 mm/s (Fig. 2(b)). This is corresponding to a complete mixing with a mixing efficiency of 99.45% and a mixing time of 0.19 s, where the mixing time equals mixing microchannel length divided by the fluid velocity for each flow rate, The mixing efficiency and mixing time were 99.6% and 0.21 s, respectively, at a flow rate of 0.5 μl/min (Fig. 2(c)). We validated these flow rates experimentally. We have applied a pressure of 6 Pa to the inlets, which corresponds to a flow rate of 0.6 μl/min. Experimentally, we injected the fluidic with a fixed flow rate. It is noted that the degree of mixing was assessed at the end of the focusing region (just before the first impedance measurement), which is indicated by the black circle in Fig. 2(a). The majority of fluid mixing happened in the mixing region. However, the fluid continued to be mixed in the focusing region. At higher flow rate the mixing time was decreased but this resulted in lower mixing efficiency, e.g., at a flow rate of 0.8 μL/min, the mixing efficiency was ~89% and mixing time was ~0.14 s.

2.2. Microfluidic sensor focusing channel modeling

The ramp down focusing channel (length 800 μm), contains a metallic (gold) vertical electrode and thin narrow finger pairs tilted with 45° and made of chromium (Cr) and gold (Au), and a ramp down SU-8 negative photoresist microchannel. This region has a starting and ending width of 100 μm and 12 μm, respectively. The fingers' widths were 10 μm, and the spacing between them was 10 μm. The edge-to-edge distance between each finger pair was 12 μm. In modeling using COMSOL finite element tool, the electric field (E-Field) intensity and its gradient were simulated across the focusing electrodes using AC voltage at a specific frequency with the purpose of maximizing the E-field intensity and gradient across the centerline of the microchannel while reducing them elsewhere. The finger tilting angle as well as the ramp down angle of the microchannel/vertical electrode pair were varied until optimum focusing electrode dimensions, AC voltage and frequency values are obtained. The results demonstrated that when an alternating voltage, V_{p-p}, at an optimum frequency in the mega Hz value is applied across the focusing region, a non-uniform E-field is generated with its strongest intensity and gradient are in the center of the microchannel between the finger pairs edges and decreased significantly while moving away towards the microchannel walls. The combination of metallic vertical side wall and finger pairs with thin Au film generated p-DEP forces that move and focus the cells/particles, e.g., the RBCs single file into the center of the microchannel, providing excellent focusing capability to prevent clogging in the device. In addition, the device can focus the cells at any location across the microchannel height due to the use of vertical electrode pairs (Fig. 2(d)). Initially, the tilted thin film finger pairs generated stronger p-DEP forces, dominating the focusing process because the vertical sidewalls were far from each other, and thus focusing the cells in a narrow line in the center. As the microchannel ramped down, the generated p-DEP force from the vertical electrode pair become dominants especially in the z-axis and contributed more to the focusing process. Finally, the ramp down feature of the microchannel generated hydrodynamic forces that also aided the focusing process. However, the hydrodynamic forces alone were not able to focus the cell into the centerline unless the microchannel is very long, which is not possible for the current application.

2.3. Cell sensing region modeling

The sensing region (length 20 mm, width 12 μm) is populated with

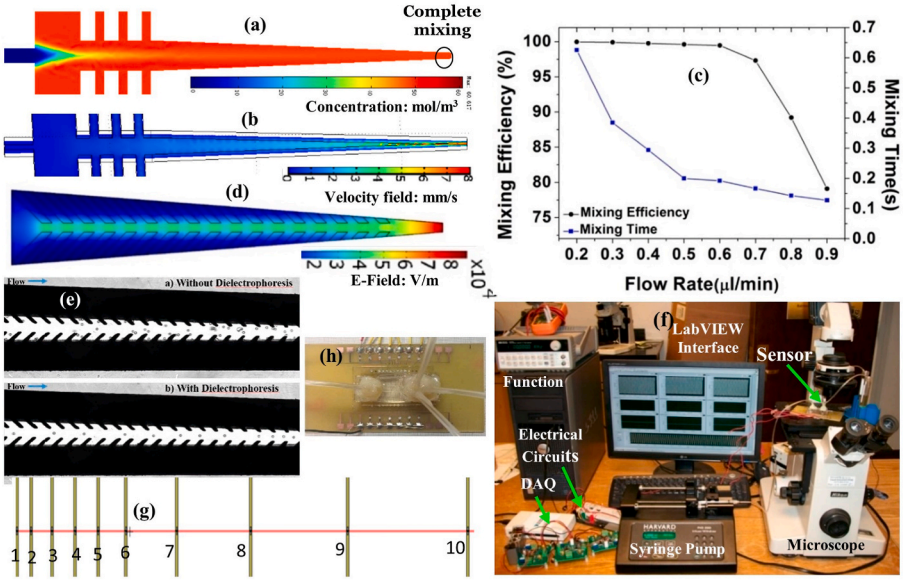

Fig. 2. (a) COMSOL modeling and simulation of (a) passive mixing of two dyes. The uniform color at the end of the mixing region, represents complete mixing. (b) Fluid speed in the microchannel. The fluid velocity in the straight part of the microchannel was increased from 3 mm/s to 8 mm/s, with an average speed of 5.5 mm/s. (c) Mixing efficiency and time vs. flow rate. An efficiency of 99.5% and mixing time of 0.22 s were achieved at 0.5 μl/min. (d) Electric field intensity simulation. (e) The beads were aligned and observed using an optical microscope. (f) Testing setup, (g) The 10 electrodes distribution along the channel length, (h) a sample of a tested device on PCB board. (For interpretation of the references to color in this figure legend, the reader is referred to the Web version of this article.)

ten vertical gold electroplated electrode pairs, fabricated by electroplating gold. The electrode geometry (width 40 μm, length 30 μm) was chosen to minimize the chances of having two cells passes at the same time, and to achieve a uniform E-field as a function the microchannel's height. In addition, the small width between the electrode pairs increases the impedance change, necessary to maximize the sensitivity. The transit time between the first and last electrode pairs impedance measurement was 0.8 s at 0.5 μl/min flow rate.

The voltage across each electrode pair was measured with and without a cell/microbead flowing through. The difference indicates the voltage change (ΔV), which is used to calculate the impedance change (ΔZ), for each electrode pair of the 10 electrodes. The voltage and impedance change are related by

$$\frac{\Delta Z}{Z_{ch}} = \frac{\Delta V}{V_{ch} G_{amp}}, \tag{8}$$

where Z_{ch} and V_{ch} are the measured impedance and voltage of an electrode without a cell, and G_{amp} is the amplifier gain.

3. Fabrication

The biosensor was built on glass slides/substrates as follow (Fig. 1 (b)). The slide was first cleaned thoroughly to wash away all particles, dirt, and contaminants using the standard piranha for 5 min, i.e., H_2O_2 and H_2SO_4 at a ratio of 1:3 and DI water. The fabrication includes the following processing steps. The substrate was coated with a negative SU-8 2005 photoresist, prebaked on hotplate at two temperatures 66 ± 1 °C and 96 ± 1 °C for 1 min and 2 min, aligned and exposed to ultraviolet light using the MA6/BA6 mask aligner for 25 s, and post baked at two temperatures 66 ± 1 °C and 96 ± 1 °C for 30 s and 1.5 min, respectively. This is followed by hard baking the SU-8 layer at 150 °C for 40 min removing all solvents from the SU-8 layer and achieve a thickness between 4 and 5 μm. The SU-8 2005 layer is crucial to enable the subsequent microfluidic channel, i.e., made of SU-8 2025 to stick to the slide/glass-substrate. (2) A Au film (150 nm) was sputter-deposited and patterned to create the focusing and sensing regions. A Cr layer (55 nm) was used as an adhesion layer. The Au layer was also used to enable electroplating the vertical regions of the electrode with Au thick layer (Fig. 1(a)).

A step toward creating the focusing and sensing regions vertical sidewalls, a micromold was patterned using AZ 4620 photoresist (thickness 25 μm) and was filled with electroplated Au using a plating solution, heated at 55 °C and stirred at 65 RPM. We have applied 55 μA current to generate the electroplating inside the micromold. After electroplating is completed the photoresist micromold was flushed and removed with acetone and cleaned IPA. Next, the Cr thin film was not needed anymore and was removed using wet Cr etchant. The channel was formed by patterning SU-8 2025 negative photoresist. A SU-8 2005 was spin-coated, prebaked on hotplate at two temperatures 66 ± 1 °C and 96 ± 1 °C for 1.5 min and 4 min exposed to ultraviolet light for 9 s, then was baked at 66 ± 1 °C and 96 ± 1 °C for 2 min and 5 min, respectively. Finally, it was baked at higher temperature, i.e., 150 ± 1 °C for 30 min to achieve a height of 28 μm (Fig. 1(b)).

Finally, the SU-8-2025 was covered with 2 layers of thick Polydimethylsiloxane (PDMS) to seal and form the sensor. The first PDMS layer was loaded inside Oxford Reactive Ion etching system and plasma was generated in an oxygen environment. This step modified the PDMS layer from hydrophobic to a hydrophilic. A SU-8 2005 thin layer was added on the PDMS surface, placed on a hotplate, and heated for 10–15 min. This step is important to achieve excellent adhesion of PDMS layer to the SU-8 microchannel on the substrate.

The PDMS slab was aligned on top of the SU-8 microchannel and heated on a hotplate at 45 °C for 12 min. A 0.5 kg was placed on the PDMS to strengthen the adhesion. Another slab of PDMS was prepared using the same procedure but with microfluidic connectors and tubes. This layer fixed to the first PDMS slab (Fig. 2(h)), and the device was fixed on a pre-prepared PCB with a window at its center to allow observing the device via backside microscope. Fig. 1 shows side-view schematics and SEMs of the sensors.

4. Materials and methods

4.1. Testing setup

The sensor was operated using couple of syringe pumps and 3 mL Syringes (BH Supplies), couple of standard function generators, a DC power supply (Agilent E3646A), and a custom-made electrical circuit were employed to test and record the impedance changes of RBCs, beads and other types of particles (Fig. 2(f)). The syringe pumps were used for the purpose of injecting the RBCs or calibration beads from the fluidic inlet connected to the center channel and extracellular media, e.g., PBS, into two fluidic inlets connected to the outer channels. A function generator applies an alternating peak to peak voltage of 6 V at 10 MHz, to produce positive dielectrophoresis forces across the focusing electrode pair. A second function generator applies AC voltage across the sensing electrode pairs. The voltages across the 5 sensing electrode pairs (1, 2, 3, 6, and 10) were measured and recorded using Labview and a DAQ board (National Instrument), while RBCs or microbeads were flowing through the microchannel. An instrumentation amplifier amplifies the measured signal which was filtered. An optical microscope was used to inspect the microchannel and to observe the mixing, focusing and sensing regions while the RBCs, or microbeads flowing in the microchannel.

4.2. Testing of cell/bead focusing

The focusing electrode pair's ability to line up the beads/RBCs in the centerline of the channel was tested experimentally using beads with a diameter of 5 μm, and by applying a Vp-p voltage of 5 V at 5 MHz, as shown in Fig. 2(e) before and after applying p-DEP effect. The experimental results demonstrated that without the use of focusing effects the microbeads were flowing randomly everywhere, without being focused. The focusing effects happened only after applying an optimum AC voltage at a specific frequency. The voltage and frequency were determined experimentally using microbeads.

4.3. Red blood cell sample preparation

The animal use for the collection of RBCs was approved by the University of Missouri's Animal Care and Use Committee. The rats were housed at a temperature range of 20–22 °C and lighting (10-h dark/14 h light) controlled environment and provided free access to water and standard pelleted rodent chow. Whole blood was withdrawn from 3 to 4 months old Sprague Dawley rats using 18-gauge needle by cardiac puncture post-euthanasia with CO_2 inhalation. The whole blood was then transferred into a tube containing Ethylenediamine Tetraacetic Acid (EDTA) solution and centrifuged at 500×*g* force for 10 min at 4 °C. The supernatant was removed, and RBCs were resuspended to twice the pellet volume in Dulbecco's phosphate-buffered saline (PBS, Sigma Aldrich). RBCs were then centrifuged at 500×*g* force for 10 min at 4 °C, and the supernatant was discarded again, and RBCs were resuspended in double the volume of PBS. The previous two steps were repeated two more times for a total of 3 washes of the RBCs [32]. Usually, 0.5 mL RBCs were extracted and suspended in 15 mL of media for testing.

Studies with human RBCs were exempt from Human Studies consideration because the cells were de-identified by the Red Cross before provision.

4.4. Bead diameter-voltage response

To identify the diameter-voltage response in our new device, we

measured the impedance at 1.0 kHz of latex beads (Sigma-Aldrich) with nominal diameters between 4 and 8 μm contained in 1x PBS using 5 electrodes. Briefly, beads for each diameter were diluted in 1x PBS. Each of the bead suspensions was then injected into the cell-inlet and 1x PBS was loaded into the media inlets (Fig. 1) at 0.5 μl/min in each inlet. Voltage time series were collected at each electrode pair, and individual beads were tracked due to the consistent inter-electrode time steps. To establish the voltage diameter relationship, a linear regression was performed on mean bead voltages. To establish the mean coefficient of variation among electrodes along the channel for repeated bead measurements, we found the mean of the coefficients of variation for each bead diameter:

$$E(\mathrm{CV}) = \frac{1}{n}\sum_{i=1}^{n}\frac{\sigma_i}{\mu_i}, \tag{9}$$

where n is the total number of beads observed, and μ_i and σ_i are the mean and standard deviation of the measured voltages along the five electrodes for bead i.

4.5. RBC equilibrium volume-voltage response

Rat RBC were collected as described above. However, in the final step here RBC were resuspended in one of 1x, 1.5x, 2x, 3x, or 5x PBS solutions prepared from 10x PBS stock solution (Sigma-Aldrich). Then the RBC suspension was injected into the cell-inlet and the corresponding xPBS solution was injected into the media inlet (Fig. 1) at 0.5 μl/min in each inlet. Voltage time series were collected at each electrode pair, and individual RBCs were tracked due to the consistent inter-electrode time steps. To establish the voltage diameter relationship, a linear regression was performed on mean RBC voltages as a function of inverse osmolality (a Boyle van 't Hoff plot; Fig. 4). To establish the mean coefficient of variation among electrodes along the channel for repeated RBC measurements on fully equilibrated RBC, we found the mean of the coefficients of variation for each RBC using Eq. (9).

4.6. RBC dynamic volume-voltage response

Rat RBC were collected as described above. However, in the final step here RBC were resuspended in 1x PBS. Then the RBC suspension was injected into the cell-inlet and 1.5x PBS solution was injected into the media inlet (Fig. 1) at 0.5 μl/min in each inlet. Voltage time series were collected at each electrode pair, and individual RBCs were tracked due to the consistent inter-electrode time steps.

To identify RBC permeability, we assumed that the extracellular osmolality experienced by a RBC under steady state conditions was parameterized by the equation informed by our COMSOL simulations

$$\pi(t) = (0.5\sigma((t-0.17)/b]+1)\pi_0 \tag{1}$$

where

$$\sigma(z) = (1+\exp(-z))^{-1},$$

b is a fitting parameter, and π_0 is isomolality (0.29 osm/kg). This equation was coupled with a solvent flux model [33]

$$\frac{dw}{dt} = -L_p ART\left(\pi(t) - \frac{w_0\pi_0}{w(t)}\right) \tag{2}$$

where w and w_0 are the volume of intracellular water *and* at isosmolal conditions, respectively, L_p hydraulic conductivity, A surface area (assumed constant), R gas constant, and T temperature, and values are given in Table 1. For this experiment, equation (1) has the initial condition, $w(0) = w_0$, and the total RBC volume is given by

$$v(t) = \frac{w(t)}{1-v_b},$$

Table 1
Table of parameters and reference values.

Parameter	Description	Units/Value/ Reference
ΔV	Change in voltage due to a particle	volts
Z_{ch}	Baseline impedance without a cell/particle	ohms
V_{ch}	Baseline voltage without a cell/particle	volts
G_{amp}	Amplifier gain	Unitless
$\pi(t)$	Extracellular osmolality experienced by RBC	osm/kg
π_0	Isosmolality (osmolality at isotonicity)	0.290 osm/kg
$\sigma(z)$	Sigmoidal function	
w	Intracellular water volume	μm^3
w_0	Isosmotic water volume	30.3 μm^3
v_b	Osmotically inactive volume fraction	0.55
L_p	Hydraulic conductivity	μm/min/atm
A	RBC surface area	115 μm^2
R	Gas Constant	0.083 L atm/(K mol)
T	Temperature	295.12 K

where v_b is a known or measured osmotically inactive cell volume fraction [34]. The parameters b was determined by solving the hierarchical optimization problem:

$$\min_b\left\{\min_{L_\mathrm{p}} SSE(L_\mathrm{p}; b)\right\},$$

where *SSE* is the sum of squared errors of measured vs predicted total cell volumes, normalized such that the cell was assumed to be in complete equilibration at time $t = 1$ s, an assumption supported by predictions informed by human RBC literature data (data not shown). Given b, the measured values of L_p were those that minimized the sum of squares for each individual RBC The optimization problem was solved using Mathematica (v. 12.3; Wolfram, Inc).

4.7. Malaria detection

Plasmodium falciparum-infected RBC (strain 3D7) were cultured in RPMI medium supplemented with Albumax as previously described. Red blood cells were obtained from the American Red Cross Blood Services (St Louis, MO). On separate days for each treatment, we spiked healthy RBC with either ring stage infected RBC (from the same donor) at a parasitemia level of 5%, 10%, or 15%, or schizont stage infected RBC at a parasitemia level of 10%. After spiking and suspending in PBS, we injected these into the center channel of our device and injected 10% DMSO into the outer channels. Measurements were recorded until at least 60 events were logged. All ring stage trials were conducted once each on separate days, the schizont stage trials were conducted twice on two separate days. Dynamic volumes for these mixtures were tested and recorded at 5 electrode pairs. Comparisons of counts of presumed infected cells (clearly separated by voltage) vs expected parasitemia rates were conducted using the χ^2 statistic.

5. Results and discussion

We designed, fabricated, and validated a novel microfluidic sensor using both beads and RBCs. To our knowledge there have been no reports of the time dependence of individual RBC responses to osmotic challenge. The data facilitated by this device will allow for innovation in RBC quality assessment, including measurement of membrane integrity, sphericity, and membrane lipid composition. Importantly, these measurements can be made at the individual cell level allowing for novel study and identification of subpopulations of cells. The osmotic behavior of these subpopulations may be reflective of the natural RBC cycle, subpopulations susceptible to storage lesion or cryoinjury, or even pathologies such as malarial infection.

In this manuscript we presented the design of a device to enable its application with rapidly responding individual RBCs that can be fully

equilibrated in anisosmotic medium in less than 1 s. Our design included a novel mixing region, that decreased total mixing time from our previously published 0.26 s to 0.19 s, while increasing the mixing efficiency from 97% to 99% as predicted by our COMSOL model (Fig. 2). COMSOL mixing efficacy was predicted by taking the mean concentration across the entire channel. However, the osmolality experienced by the cell is likely to be dominated by its position in the channel, with the majority of cells occupying the centerline of the channel. Thus, we experimentally determined the most likely concentration vs time profile experienced by cells using Eq. 1, and a global parameter fitting protocol. The determined concentration vs time curve shown in Fig. 5 is in line with our COMSOL predictions. In particular, from our experimental model, we expect 91% mixing efficiency at the centerline of the channel where the cells are located by time $t = 0.19$ s. This is in general agreement with the average mixing efficiency of 99% across the entire channel at the flow rate chosen, as shown in Fig. 2, where the majority of the channel is fully equilibrated before the first measurement occurs.

We made significant improvements to the focusing region in the current devices, and photomicrographs demonstrate that cells are nearly perfectly aligned with the center of the channel in the focusing region, as shown in Fig. 2. In fact, due to the new focusing electrode pair design, cells are more focused towards the centerline at the onset of mixing. This has the added benefit of ensuring that cells experience a repeatable extracellular osmotic environment, defined by our $\pi(t)$.

5.1. Bead diameter-voltage response

To identify the volume-voltage response of beads, we measured voltages for beads of known diameters. Fig. 3 shows the mean ± STD of the voltage recorded at 5 electrode pairs for beads with 4 different diameters. The figure shows that the mean voltage was increased linearly as a function of diameters and there was no mean difference among electrode pairs. The coefficient of determination for the linear regression of voltage on diameter was $R^2 = 0.99$. This linear voltage-diameter relationship was also reported by Richards et al. [35]. This is different from the expected conventional Coulter counter designs [36]. The mean coefficient of variation for bead voltage measurements along the five electrodes among all bead sizes was 0.0164. The bead concentration was also varied, and a (non-overlapping) throughput of 150 beads/sec was consistently achievable. The transit time between each electrode pair was measured and calibrated using the initial voltage value at each electrode pair. Then the subsequent voltages for individual microbeads were correlated with the 5 electrode pairs by this estimated transit time.

5.2. RBC equilibrium volume-voltage response

To identify the volume-voltage response of RBC, rat RBCs equilibrated in different PBS concentrations (1x, 1.5x, 3x, 5x) were injected into center inlet while the same concentration of PBS were injected from the media inlets and are presented in a Boyle van 't Hoff style plot (Fig. 4). Total observations at 1x, 1.5x, 3x, 5x were 14, 13, 12, and 11, respectively. Because the osmolality was the same in both the cell and media inlets, the RBC volume was not expected to change over time. This was borne out in the mean coefficient of variation for individual RBC voltage measurements along the five electrodes among all treatments was 0.015. We found that mean voltage increased linearly with voltage, and a regression of mean normalized voltage vs relative inverse osmolality resulted in a normalized voltage model of with coefficient of determination $R^2 = 0.92$.

$$\frac{V}{V(\pi_0)} = 0.55 + 0.47\,\frac{\pi}{\pi_0} \tag{3}$$

There is a large difference between the voltage-diameter relationship in latex beads compared with live cells in our device. The linearity of voltage and diameter in beads in a microfluidic coulter counter has been confirmed by others in the literature [35], and the linearity of voltage and volume in cells is the standard assumption for coulter counters. We believe that there are secondary electrical characteristics of beads compared to cells that must account for this. For example, latex beads should have little to no conductance in the interior space, whereas the intracellular space is highly conductive. This discrepancy in the voltage-volume relationships between beads and cells challenges the applicability of our device in some ways as it means that calibration to bead standards is not possible. However, our Boyle van 't Hoff plot showing that the relative volumes of RBCs seem to be preserved make a compelling argument that the dynamic responses of cells are at least accurate relative to themselves, and provide sufficient information for counting cells, identifying membrane intact cells, and identifying the membrane permeability of individual cells, which were design goals of our device at the outset.

Using pre-equilibrated RBC allowed us to make repeated measurements of individual RBC at defined osmolalities. This allowed us to ensure that the cells were entirely equilibrated, whereas in dynamic experiments, it was possible that cells could still be changing volume by the end of the 0.9 s time course. Rat RBCs are known linear osmometers in the range of osmolalities used in this study and our results, normalized to isosmotic voltages, our regression agrees perfectly with the previously published values obtained via photomicroscopy [37]. Our results at individual osmolalities, however, do not overlap perfectly with expectations. In particular we measured voltages at 3x PBS that were higher

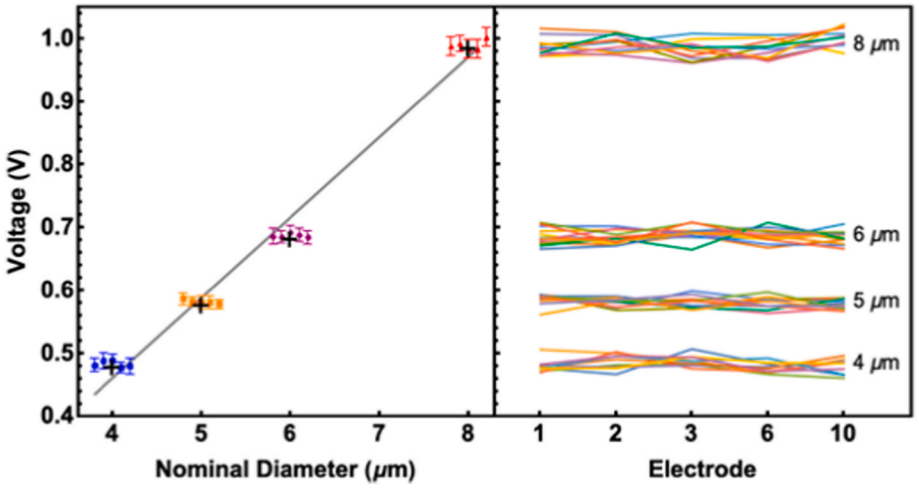

Fig. 3. (a) The voltage (mean ± SD) vs. microbead diameter. For each microbead size, individual microbeads were measured using five electrodes, which correspond to 5 means (separated in the diameter axis for clarity) at each nominal microbead size. The mean voltage at each nominal size is indicated with the + symbol. A regression of mean voltage vs diameter is shown in gray. The coefficient of determination of this regression was $R^2 = 0.988$. (b) Voltage traces of individual bead volumes through five electrode pairs. There is inherent variance in microbead diameter but the small electrode-to-electrode variance is shown by the nearly parallel traces along the channel, and the mean coefficient of variation of 1.7 ± 0.4% (mean ± SD).

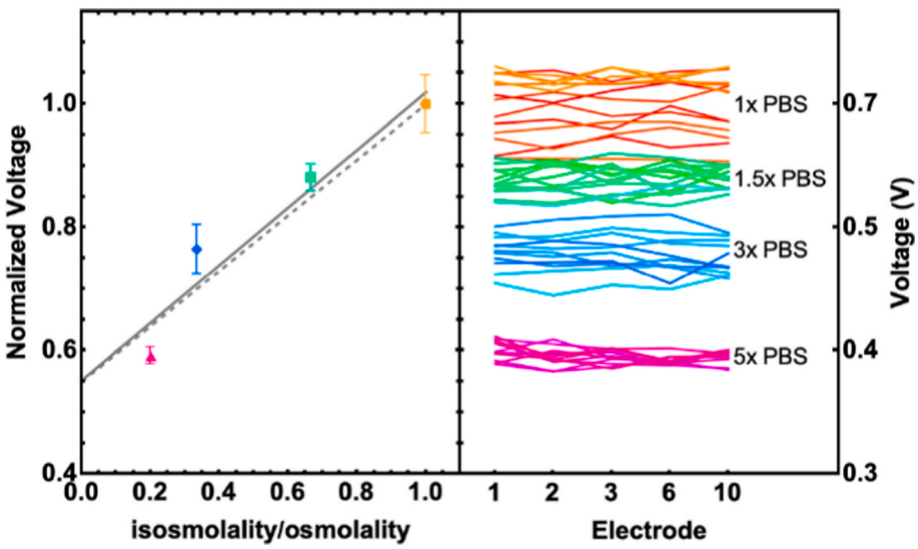

Fig. 4. (a) A Boyle van 't Hoff-like plot of normalized voltage (mean ± SD) versus relative inverse osmolality. At each osmolality (xPBS), individual RBC were measured using 5 electrodes, and the mean voltage was recorded for the population of RBC (n = 50). The solid line shows a regression of these data, with intercept v_b = 0.55 and coefficient of determination of R^2 = 0.92. The dashed line shows the expected response from the literature for rat RBC [33], which has an intercept of v_b = 0.55. (b) Voltage traces of individual RBC volumes through 5 electrodes. Colors align with the colors in plot (a). The mean coefficient of variation along 5 electrodes among all individual RBCs was 3.7 ± 1.5% (mean ± SD). The different colors are to help the reader to differentiate among traces at each PBS concentration. (For interpretation of the references to color in this figure legend, the reader is referred to the Web version of this article.)

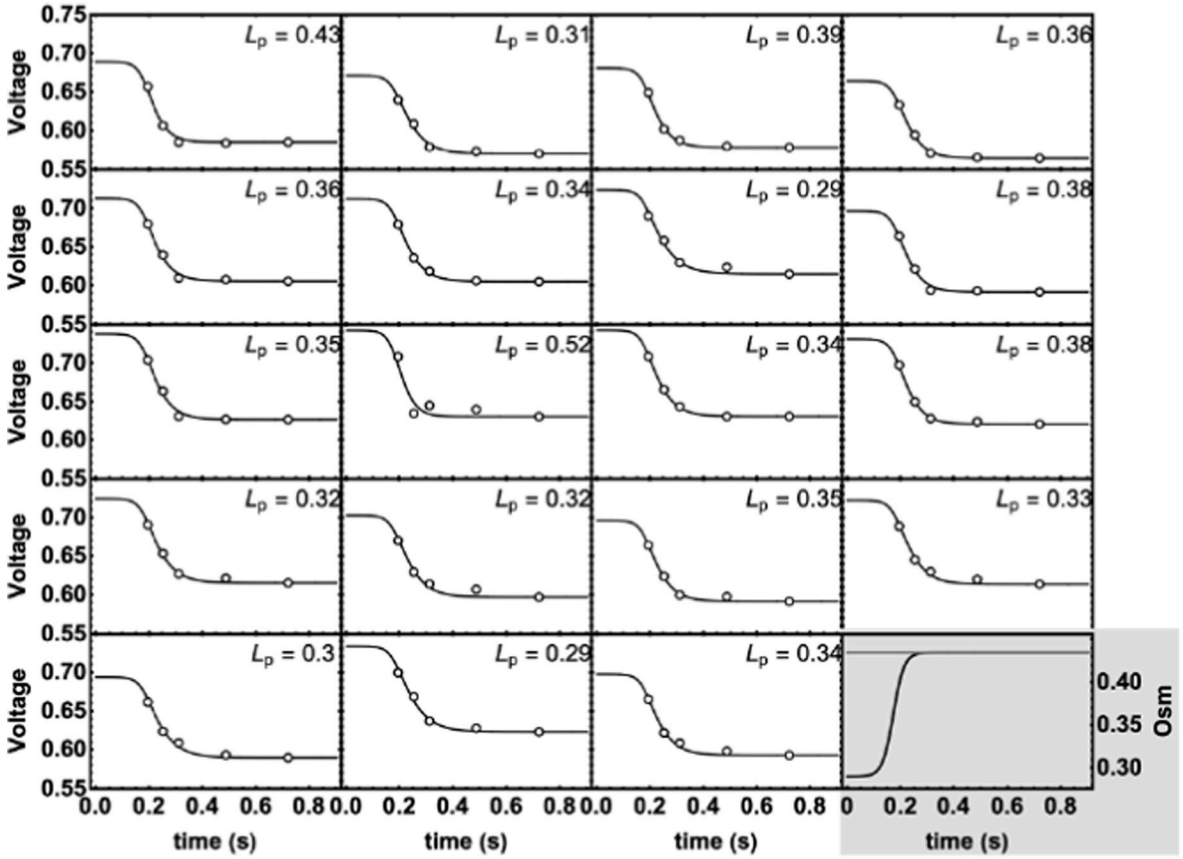

Fig. 5. Voltage responses of 19 individual RBC in 1x PBS mixed with 1.5x PBS (open circles). A best fit concentration parameter b = 0.02 was found, and the corresponding best-fit L_p for each individual RBC was found, indicated in each subplot (with units μm s^{-1} atm^{-1}). Model predicted voltage responses are shown in solid black lines. (Bottom right) Predicted osmolality (black) $\pi(t)$ in the device as a function of time experienced by individual RBC with the onset of mixing at time t = 0, described by Eq. (1) with b = 0.02. Initial concentration is 0.29 osm/kg, and final expected concentration is 0.435, indicated by the gray line.

than expected, and voltages at 5x PBS that were lower than expected. This may be due to the fact that we only obtained data for a small sample of RBC. It is an ongoing area of work to streamline the process of obtaining data from the device so that we can better achieve the throughputs obtained with beads [31]. Albeit with only one measurement channel active. An alternate explanation of the possible deviation of our measurements from expected is that the sphericity of RBC is low in isosmotic conditions and changes as water leaves the cells. In applications using RBC in benchtop Coulter counters, specific RBC calibration standards must be used to ensure accurate volume measurement [38]. This being said, we believe that in the small range of osmolalities used for our subsequent dynamic response experiments the linear relationship between voltage and volume is well justified.

5.3. RBC dynamic volume-voltage response

Red blood cells were suspended in 1x PBS and loaded into the cell inlet and mixed with 1.5x PBS from the media inlets, corresponding to an osmotic shift of 0.29 osm/kg to 0.435 osm/kg. The voltage-volume response for RBC in this narrow range of osmolalities was assumed to be linear according to Eq. (2). Individual RBC volumes from 19 RBCs were thus measured using 5 electrode pairs as shown in Fig. 5. Our results demonstrate smooth voltage changes, which indicate that the membranes of the RBCs were intact; only cells with intact membranes will respond osmotically. Our results also show the proportionality of time intervals between the measured voltage/impedance and inter-electrode distance. The best fit concentration parameter, $b = 0.02$, was found, and corresponding best-fit L_p were found for each individual RBC. A plot of the predicted extracellular osmolality $\pi(t)$ is shown in Fig. 5. The mean value for L_p was 0.35 ± 0.054 (mean ± SD), and the mean coefficient of determination for all fits was $R^2 = 0.98 \pm 0.027$ (mean ± SD).

We fit the volume responses of 19 RBC exposed to 1.5x PBS using a simple and standard water transport model [38]. To do this we needed to determine a parameter to describe the extracellular osmolality experienced by individual RBC as a function of time in the mixing region before the first measurement of volume. This was done by fitting a one parameter sigmoidal function to the full dataset. The resulting concentration vs time curve shown in Fig. 5 aligns well with expectations for the concentration at the centerline of the device, where the majority of cells will be during the experiment. While more complex or multiparameter candidate functions for the concentration at the centerline could be suggested, we wanted to minimize overfitting of our data, as each dataset only has five points in the time series.

Our fits for hydraulic conductivity for human RBC are in general agreement with data published previously. To our knowledge, there have been no publications of rat RBC permeabilities to water. In particular, Lahmann et al. [33] suggest that if the osmotic change goes from 0.29 mosm/kg to 0.435 mosm/kg (as studied in our experiments), the water permeability of human RBC should be 0.67 μm/min/atm, compared to the mean value of 0.35 μm/min/atm obtained for rat RBC in the current manuscript. This discrepancy could be due to interspecies differences in aquaporin expression, or significant differences in RBC mean corpuscular volume and surface area which are around 2/3 the values in rat compared to human. This discrepancy could also be attributed to the fact that there are widely varying reports of water permeability of RBC populations in the literature at these lower concentrations, and as such, the regression model that [38] use to identify expected water permeabilities as a function of osmolality may not be accurate at specific concentrations, or under specific experimental conditions. Finally, our measured osmotically inactive fraction was 0.55, which is a difference from the osmotically inactive fraction of human RBC, known to be 0.43 [33]. These slight differences between rat and human RBC should play only a minimal role in tracking RBC volumes, thus translating our work to human applications should not theoretically be a problem.

Our work is a first step towards a much more general and flexible tool for hematologists to study RBCs, both in a research setting, and in clinical applications. However, there are several areas of improvement needed for implementation. A key area of improvement is the ease of application in minimally processed samples, e.g. heparinized whole blood, or even blood drops obtained from finger pricks [39,40]. For over 70 years, Coulter counters have been used to identify and distinguish among multiple cell types within whole blood. Because of these existing Coulter counter whole blood protocols, our device should be easily translatable to be used with whole blood. Thus, a remaining critical design consideration to adapt the present device for use in human diagnostics is account for the widely varying sizes in whole blood, the relationship between channel width, mixing efficiency, and electrode pair sensitivity must also be carefully adapted so as to remain able to identify RBC quality while not being clogged with larger cell types. However, the potential for the present device to function as a "classical" Coulter counter is an added benefit, as RBC characterization is only part of a standard blood panel that identifies platelet count, white blood cell counts, etc.

We expect that the most significant obstacle to adoption, then, is the ability to improve throughput. We have determined that throughput is at least 150 samples/sec, or 9000 samples/min using microbeads, but we have not implemented this high throughput with RBCs in this study. Therefore, with careful attention to cell dilution, careful management of cells to prevent clumps of cells forming, and sufficiently homogenized cell suspensions, we anticipate that these throughputs should be achievable in cell suspensions. These higher throughputs do require improved data management and analysis considerations. We have previously shown with beads that inter-electrode timings are extremely stable, however, 150 samples/sec requires sub millisecond precision to ensure that cell *i* passing through electrode pair 1 is identified as cell *i* at each subsequent electrode.

Our work can be further improved by changing the electrode pair position configuration. It is possible to change the ratio of lengths between electrode pairs arbitrarily to allow relatively longer or shorter times between them, and to adjust the total overall length and total time by adjusting the flow rates accordingly. These considerations must be balanced with the mixing efficiency, but as we demonstrated here, phenomenological mixing curves should enable accurate estimates of dynamic responses independent of perfect mixing.

There is little in the way of using this device with whole blood products from the bag or auxiliary tube pieces (in case of a storage scenario) or μl quantities of whole blood obtained from a skin prick in the case of a clinical or field applications. For over 50 years, Coulter counters have been used to identify and distinguish among multiple cell types within whole blood. Because of the existing Coulter counter whole blood protocols, we believe that the only remaining critical design consideration in the present device is the relationship between channel width, mixing efficiency, and electrode pair sensitivity to remain able to identify RBC quality while not being clogged with larger cell types. On a different note, the hematology units that would be likely adopters of this present technology routinely isolate RBC, and as such, we initially expected that an instrument like ours and the measurements it replaces would be part of this standard workflow.

5.4. Malaria infected RBC dynamic volume-voltage response

Finally, here we present the first report of detection of malaria

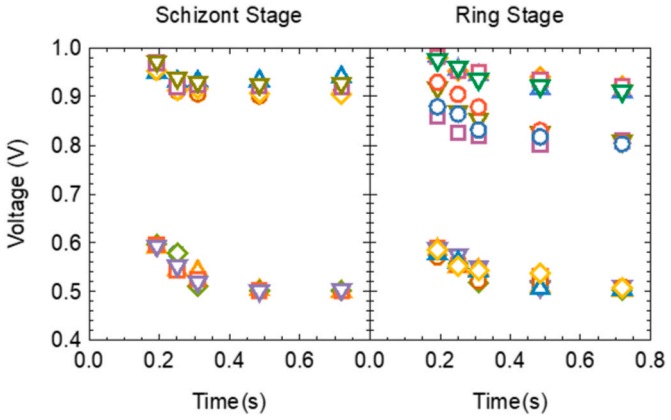

Fig. 6. Voltage versus time for schizont and ring stage iRBC mixed with uninfected RBC at 10% parasitemia. Five suspected iRBC and five suspected normal RBC traces are shown. Clear separation between suspected groups is visible at both stages. Suspected iRBC are shown in the top half of each panel with white background.

infected RBC using the Coulter principle. Example voltage traces for human RBC mixtures spiked with malaria infected RBC are shown in Fig. 6. There is an unmistakable subpopulation reflected in mean voltages that were approximately 0.4 V above the main population throughout the dynamic range. We used this mean voltage difference as a simple filter to count members of each subpopulation. The larger subpopulation was assumed to be iRBC under all treatments (Table 2), and parasitemia levels were calculated. A χ^2 statistic of measured versus expected iRBC in each sample found no difference between expected and measured counts of suspected iRBC over all five trials ($\chi^2 = 0.194$, df = 4, $p = .996$).

There was a nearly two-fold difference in the voltages measured in suspected parasite infected RBC compared with suspected healthy RBC, independent of their volume response to anisosmotic mixing solutions. These results were confirmed through varying parasitemia loads and measuring the proportion of suspected infected RBC. We strove to use as many tools to identify infected RBC as possible. In this case, we used a common highly membrane permeable chemical as the osmolyte instead of saline to make possible the use of two discriminating variables: water and solute (DMSO) permeability. However, in the current device design with its current optimal flow rate and transit time, the inward diffusion of DMSO into RBC was minimal over the time-course, the effect on RBC volume was negligible (whether control or malaria infected), and as such DMSO was treated as impermeable on this time scale. This water permeability is in agreement with reports of the response of human RBC to DMSO on these time scales [40,41].

In future studies, we will further confirm these results by using GFP labeled parasites with time-correlated microscopy and microfluidic measurement. If our validated experiment confirms that this nearly 2-fold voltage difference holds for parasite infected RBC, we will be able to make additional design choices to reduce manufacturing costs and/or increase throughput. Current RDT are accurate but rely on the detection of HRPII that is not universally present [28]. Because the alternative assessments such as microscopy or PCR are expensive and labor intensive, our device provides a resource that requires less training than microscopy, and the ability of detection at levels compared with microscopy in only few minutes. A good threshold for microscopy diagnostics is 100 parasite/μl in a span of around 10 min [30]. With our device, and a RBC concentration of 4×10^6 erythrocytes/μl, this translates to around 5 min of sample collection with our anticipated rate of 9000 RBC/min, or a doubling of throughput in a microscopy free (and thus low delay) diagnostic. This delay can be made even shorter if whole blood can be used as described above. In this scenario, little to no processing would be required before directly analyzing potential parasitemia levels in whole blood products. Additionally, throughput can be improved via testing multiple samples in parallel: a chip with two or three parallel channels could multiply throughput equivalently. Our ongoing research includes translation of these studies into devices that will facilitate inexpensive rapid RBC testing to screen for candidate malarial infection. This should aid significantly in the usability of the device in the field, and we anticipate that this will require minimal user training, as there is no need for microscopy, nor for fluorescence chemistry or other molecular biological technologies. Suspected positives can be confirmed with microscopy or gold standard PCR tests. Currently, each fluidic chip should be treated as a disposable device and for one time use for clinical application to avoid the possibility of contamination.

6. Conclusion

In this manuscript, we demonstrated the application of a novel sensor to determine biophysical characteristics for individual RBC. We expect that with refinement, this approach will provide an efficient proxy measure of the effect of the length of RBC storage in the blood bank on the measurable changes in membrane morphology, deformability, osmotic fragility, and sphericity. While useful in clinical settings where RBC are frequently isolated, we anticipate that adaptation to minimally processed whole blood. The results suggest that each chip should facilitate the analysis of the changes in the structure of thousands of blood cells per minute of interest to blood bank operators, transfusion medicine specialists and hematologists, and has promising possibilities in application to detection of malaria infected cells without the need for microscopy, fluorescence detection, or other expensive, training intensive, and time consuming approaches.

Table 2
Detection rates at varying parasitemia levels and stages. S=Schizont, R = Ring, iRBC = malaria infected red blood cells, P = Number of Presumed infected RBC, E = Number of Expected infected RBC. $\chi^2 = \sum (P-E)^2/E = 0.194$ with df = 4 yields a p value of .996.

Stage	E/total RBC	P/total RBC
S	10%	9/97 = 9.3%
S	10%	6/57 = 10.5%
R	5%	5/114 = 4.4%
R	10%	9/86 = 9.4%
R	15%	10/73 = 13.6%

CRediT authorship contribution statement

Lining Huang: Modeling and simulation, mask design, fabrication, Investigation, Validation, Data curation, and analysis, Writing – original draft, Writing – review & editing. **Ibrahim Jasim:** Contributed to fabrication, and Malaria testing. **Omar Alkorjia:** Malaria testing. **Cansu Agca:** Sample preparation for Red Blood Cells study. **Anna Oksman:** Sample preparation for malaria testing. **Yuksel Agca:** Methodology, Sample preparation, Writing – review & editing. **Daniel E. Goldberg:** Methodology, Resources, Supervision, Writing – original draft, Writing – review & editing. **James D. Benson:** Conceptualization, Funding acquisition, Methodology, Project administration, Resources, Supervision, Writing – original draft, Writing – review & editing. **Mahmoud Almasri:** Conceptualization, Funding acquisition, Methodology, Project administration, Resources, Supervision, Writing – original draft, Writing – review & editing.

Declaration of competing interest

The authors declare that they have no known competing financial interests or personal relationships that could have appeared to influence the work reported in this paper.

Data availability

Data will be made available on request.

Acknowledgements

Funding was provided in part by the University of Missouri internal funding, the National Science and Engineering Research Council (RGPIN-2017-06346 to JB), and the Saskatchewan Health Research Foundation (to JB). The last two authors contributed equally.

References

[1] World Health Organization (WHO), Global Database on Blood Safety: Summary Report 2009, 2009. https://www.who.int/publications/m/item/gdbs-summary-report-2009. (Accessed 14 March 2022).
[2] A.D. Alessandro, A.D. Gray, Z.M. Szczepiorkowski, K. Hansen, L.H. Herschel, L. J. Dumont, Red blood cell metabolic responses to refrigerated storage, rejuvenation, and frozen storage, Transfusion 57 (2017) 1019–1030, https://doi.org/10.1111/trf.14034.
[3] G. Zallen, E.E. Moore, D.J. Ciesla, M. Brown, W.L. Biffl, C.C. Silliman, Stored red blood cells selectively activate human neutrophils to release IL-8 and secretory PLA2, Shock 13 (2000) 29–33, https://doi.org/10.1097/00024382-200013010-00006.

[4] C. Morgan, T.L. Berezina, S.B. Zaets, C.R. Spillert, M. Kamiyama, Z. Spolarics, E. A. Deitch, G.W. Machiedo, Influence of storage on red blood cell rheological properties, J. Surg. Res. 102 (1) (2002) 6–12, https://doi.org/10.1006/jsre.2001.6306.
[5] R. Almizraq, J.R. Tchir, J.L. Holovati, J.P. Acker, Transfusion, undefined, Storage of red blood cells affects membrane composition, microvesiculation, and in vitro quality, Transfusion 53 (2013) 2258–2267, https://doi.org/10.1111/trf.12080, 2013.
[6] G. Deplaine, L. Safeukui, F. Jeddi, F. Lacoste, V. Brousse, S. Perrot, S. Biligui, P. A. Buffet, P.H. David, O. Mercereau-Puijalon, N. Mohandas, G. Milon, D. Mazier, M. Thellier, F. Paye, D. Cazals Hatem, C. Guitton, S. Dokmak, B. Aussilhou, A. Sauvanet, M. Guillotte, The sensing of poorly deformable red blood cells by the human spleen can be mimicked in vitro, Blood 117 (8) (2011) 88–95, https://doi.org/10.1182/blood-2010-10-312801.
[7] S.M. Frank, B. Abazyan, M. Ono, C.W. Hogue, D.B. Cohen, D.E. Berkowitz, P. M. Ness, V.M. Barodka, Decreased erythrocyte deformability after transfusion and the effects of erythrocyte storage duration, Society of Cardiovascular Anesthesiologist 116 (5) (2013) 975–981, 2013.
[8] R.T. Card, Red cell membrane changes during storage, Transfus. Med. Rev. 2 (1988) 40–47, https://doi.org/10.1016/S0887-7963(88)70030-9.
[9] B.M. Cooke, N. Mohandas, R.C. Coppel, Malaria and the red blood cell membrane, Semin. Hematol. 41 (2) (2004) 173–188, https://doi.org/10.1053/j.seminhematol.2004.01.004.
[10] A.M. Dondorp, B.J. Angus, K. Chotivanich, K. Silamut, R. Ruangveerayuth, M. R. Hardeman, P.A. Kager, J. Vreeken, N.J. White, Red blood cell deformability as a predictor of anemia in severe falciparum malaria, Am. J. Trop. Med. Hyg. 60 (5) (1999) 733–737.
[11] A.G. Maier, B.M. Cooke, A.F. Cowman, L. Tilley, Malaria parasite proteins that remodel the host erythrocyte, Nat. Rev. Microbiol. 7 (2009) 341–354.
[12] R.E. Waugh, M. Narla, C.W. Jackson, T.J. Mueller, T. Suzuki, R.G.L. Dale, Rheologic properties of senescent erythrocytes: loss of surface area and volume with red blood cell age, Blood 79 (5) (1992) 1351–1358.
[13] C. Stoll, H. Stadnick, O. Kollas, J.L. Holovati, B. Glasmacher, J.P. Acker, W. F. Wolkers, Liposomes alter thermal phase behavior and composition of red blood cell membranes, Biochim. Biophys. Acta 1808 (2011) 474–481, https://doi.org/10.1016/j.bbamem.2010.09.012.
[14] B. Bicalho, J.L. Holovati, J.P. Acker, Phospholipidomics reveals differences in glycerophosphoserine profiles of hypothermically stored red blood cells and microvesicles, Biochim. Biophys. Acta, Biomembr. 1828 (2) (2013) 317–326, https://doi.org/10.1016/j.bbamem.2012.10.026.
[15] J.D. Benson, A.J. Kearsley, A.Z. Higgins, Mathematical optimization of procedures for cryoprotectant equilibration using a toxicity cost function, Cryobiology 64 (3) (2012) 144–151, https://doi.org/10.1016/j.cryobiol.2012.01.001.
[16] J.M. Lahmann, C.C. Sanchez, J.D. Benson, J.P. Acker, A.Z. Higgins, Implications of variability in cell membrane permeability for design of methods to remove glycerol from frozen-thawed erythrocytes, Cryobiology 92 (2020) 168–179, https://doi.org/10.1016/j.cryobiol.2020.01.006.
[17] J.P. Acker, J. Pasch, I. Heschel, G. Rau, L.E. McGann, Comparison of optical measurement and electrical measurement techniques for the study of osmotic responses of cell suspensions, Cryo-letters 20 (5) (1999) 315–324.
[18] S.W. Levin, R.L. Levin, A.K. Solomon, Improved stop-flow apparatus to measure permeability of human red cells and ghosts, J. Biochem. Biophys. Methods 3 (5) (1980) 255–272, https://doi.org/10.1016/0165-022X(80)90007-X.
[19] M. Zhurova, A. Olivieri, A. Holt, J.P. Acker, A method to measure permeability of red blood cell membrane to water and solutes using intrinsic fluorescence, Clin. Chim. Acta 431 (2014) 103–110, https://doi.org/10.1016/J.CCA.2014.01.045.
[20] WHO Organization, World Malaria Report 2020: 20 Years of Global Progress and Challenges, 2018.
[21] WHO Organization, World Malaria Report 2021, 2021.
[22] S. Yongkiettrakul, W. Jaroenram, N. Arunrut, W. Chareanchim, S. Pannengpetch, R. Suebsing, W. Kiatpathomchai, W. Pornthanakasem, Y. Yuthavong, D. Kongkasuriyachai, Application of loop-mediated isothermal amplification assay combined with lateral flow dipstick for detection of Plasmodium falciparum and Plasmodium vivax, Parasitol. Int. 63 (6) (2014) 777–784, https://doi.org/10.1016/j.parint.2014.06.004.
[23] A.K. Verma, P.K. Bharti, A. Das, HRP-2 deletion: a hole in the ship of malaria elimination, Lancet Infect. Dis. 18 (2018) 826–827, https://doi.org/10.1016/S1473-3099(18)30420-1.
[24] M. Gendrot, R. Fawaz, J. Dormoi, M. Madamet, B. Pradines, Genetic diversity and deletion of Plasmodium falciparum histidine-rich protein 2 and 3: a threat to diagnosis of P. falciparum malaria, Clin. Microbiol. Infection 25 (5) (2019) 580–585, https://doi.org/10.1016/j.cmi.2018.09.009.
[25] D. Gamboa, M.F. Ho, J. Bendezu, K. Torres, P.L. Chiodini, J.W. Barnwell, S. Incardona, M. Perkins, D. Bell, J. McCarthy, Q. Cheng, A large proportion of P. falciparum isolates in the Amazon region of Peru lack pfhrp2 and pfhrp3: implications for malaria rapid diagnostic tests, PLoS One 5 (1) (2010) e8091, https://doi.org/10.1371/JOURNAL.PONE.0008091.
[26] Q. Liu, J. Nam, S. Kim, C.T. Lim, M.K. Park, Y. Shin, Two-stage sample-to-answer system based on nucleic acid amplification approach for detection of malaria parasites, Biosens. Bioelectron. 82 (2016) 1–8.
[27] M. Jauset-Rubio, M. Svobodová, T. Mairal, C. McNeil, N. Keegan, A. Saeed, M. N. Abbas, M.S. El-Shahawi, A.S. Bashammakh, A.O. Alyoubi, Ultrasensitive, rapid and inexpensive detection of DNA using paper based lateral flow assay, Sci. Rep. 6 (1) (2016) 1–10.
[28] P.K. Bharti, H.S. Chandel, A. Ahmad, S. Krishna, V. Udhayakumar, N. Singh, Prevalence of pfhrp2 and/or pfhrp3 gene deletion in plasmodium falciparum population in eight highly endemic states in India, PLoS One 11 (2016), https://doi.org/10.1371/JOURNAL.PONE.0157949.
[29] P. Berzosa, A. de Lucio, M. Romay-Barja, Z. Herrador, V. González, L. García, A. Fernández-Martínez, M. Santana-Morales, P. Ncogo, B. Valladares, M. Riloha, A. Benito, Comparison of three diagnostic methods (microscopy, RDT, and PCR) for the detection of malaria parasites in representative samples from Equatorial Guinea, Malar. J. 17 (2018) 333, https://doi.org/10.1186/s12936-018-2481-4.
[30] A. Amir, F.W. Cheong, J.R. De Silva, Y.L. Lau, Diagnostic tools in childhood malaria, Parasites Vectors 11 (2018) 1–12, https://doi.org/10.1186/S13071-018-2617-Y.
[31] L. Huang, J.D. Benson, M. Almasri, Microfluidic measurement of individual cell membrane water permeability, Anal. Chim. Acta 1163 (2021), 338441, https://doi.org/10.1016/J.ACA.2021.338441.
[32] M.S. Hanson, A.H. Stephenson, E.A. Bowles, M. Sridharan, S. Adderley, R. S. Sprague, Phosphodiesterase 3 is present in rabbit and human erythrocytes and its inhibition potentiates iloprost-induced increases in cAMP, Am. J. Physiol. Heart Circ. Physiol. 295 (2) (2018) H786–H793, https://doi.org/10.1152/AJPHEART.00349.2008.
[33] J.M. Lahmann, J.D. Benson, A.Z. Higgins, Concentration dependence of the cell membrane permeability to cryoprotectant and water and implications for design of methods for post-thaw washing of human erythrocytes, Cryobiology 80 (2018) 1–11, https://doi.org/10.1016/j.cryobiol.2017.12.003.
[34] X.S. Yang, K. Kamino, Photometric determination of phenomenological correlation between osmotic behavior and hemolysis of red blood cells, Jpn. J. Physiol. 45 (1995) 723–741, https://doi.org/10.2170/JJPHYSIOL.45.723.
[35] A.L. Richards, M.D. Dickey, A.S. Kennedy, G.D. Buckner, Design and demonstration of a novel micro-Coulter counter utilizing liquid metal electrodes, J. of micromechanics and Microengineering 22 (11) (2012), 115012, https://doi.org/10.1088/0960-1317/22/11/115012.
[36] R. Pethig, Dielectrophoresis: status of the theory, technology, and applications, Biomicrofluidics 4 (2010), https://doi.org/10.1063/1.3456626.
[37] X.S. Yang, K. Kamino K, Photometric determination of phenomenological correlation between osmotic behavior and hemolysis of red blood cells, Jpn. J. Physiol. 45 (5) (1995) 723–741, 1995.
[38] J.M. Lahmann, C. Cruz Sanchez, J.D. Benson, J.P. Acker, Implications of variability in cell membrane permeability for design of methods to remove glycerol from frozen-thawed erythrocytes, Cryobiology 92 (2020) 168–179.
[39] J.M. Moon, D.M. Kim, M.H. Kim, J.Y. Han, D.K. Jung, Y.B. Shim, A disposable amperometric dual-sensor for the detection of hemoglobin and glycated hemoglobin in a finger prick blood sample, Biosens. Bioelectron. 91 (2017) 128–135, https://doi.org/10.1016/J.BIOS.2016.12.038.
[40] J. Brahm, Diffusional water permeability of human erythrocytes and their ghosts, J. Gen. Physiol. 79 (5) (1980) 791–819.
[41] T. Papanek, The Water Permeability of the Human Erythrocyte in the Temperature Range+ 25Cİ to-10Cİ, Doctoral Dissertation, Massachusetts Institute of Technology, 1978.